
Attenuation Correction of Thallium SPECT Using Differential Attenuation of Thallium Photons

Christopher L. Hansen and Jeffrey A. Siegel*

Departments of Medicine and Diagnostic Imaging, Temple University Hospital, Philadelphia, Pennsylvania

The greatest limitation of ^{201}Tl for the diagnosis of coronary artery disease remains the high soft-tissue attenuation of its low energy photons. However, thallium also emits a smaller number of higher energy photons. Since photons of higher energy undergo less attenuation, it was postulated that the amount of attenuation could be ascertained from the ratio of the low-to-high energy photon counts. A planar phantom was used to derive a regression equation relating attenuation to the count ratio of the low and high energy peaks. A three-dimensional heart phantom was constructed and SPECT images were obtained in air and water. Application of the attenuation correction algorithm to the SPECT images of the phantom in water produced images quantitatively similar to that obtained in air. We conclude that by using differential photon attenuation, correction of ^{201}Tl SPECT using a single order post-processing technique is feasible. This technique may allow for more accurate analysis of thallium myocardial perfusion scintigraphy.

J Nucl Med 1992; 33:1574-1577

Coronary artery disease (CAD) remains the leading cause of mortality in western industrialized nations. The noninvasive evaluation of CAD relies heavily on stress testing, frequently with myocardial perfusion imaging using ^{201}Tl and single-photon emission computed tomography (SPECT). This has increased the sensitivity and specificity of stress testing to the range of 90% (1,2).

The greatest weakness of thallium is the attenuation of the low-energy mercury x-rays it produces (68.9-82.6 keV), which account for approximately 90% of the photons emitted. To partially compensate for this, many centers routinely include the higher energy photons (135 and 167 keV) also produced. Although these two photopeaks make up only a small fraction of the photons emitted, they make up a higher percentage of the photons detected due

to the fact that higher energy photons experience less attenuation.

Since the low energy x-rays undergo relatively more attenuation than the high energy photons, we postulated that the attenuation of thallium could be determined from the ratio of the detected counts from the low and high energy photopeaks. The current study was undertaken to determine whether this is feasible and whether it would allow attenuation correction of ^{201}Tl SPECT imaging.

METHODS

The study was performed in three parts. The first involved a planar phantom that was used to derive the regression equation that would correct for the attenuation of the low-energy thallium counts as a function of the ratio of the low and high photopeak counts. The second part involved construction of a simple heart phantom to determine the stability and feasibility of the regression equation in the attenuation correction of thallium SPECT. Finally, a clinical image was corrected using this technique.

The theory of the attenuation correction technique is described in the Appendix and the algorithm employed is summarized in Table 1. It was anticipated that this method would be very sensitive to image noise because it required the division of two images and the exponentiation of the result. In order to minimize this problem, it was decided to first process the high and low energy peaks using a high degree of filtering. These two images could then be used to create an attenuation correction map that would be applied to a less heavily filtered version of the low energy peak to yield the corrected image.

An annular phantom with an outer diameter of 7 cm, an inner diameter of 5 cm and 1 cm thickness was filled with approximately 200 μCi (7.4 MBq) of ^{201}Tl . The phantom was placed 22.5 cm from the face of a scintillation camera equipped with a low-energy, parallel-hole collimator. Two simultaneous image data sets were obtained. The first employed a 25% window centered on the low energy photopeak. The second consisted of two 20% windows centered on the 135 and 167 keV photopeaks.

Multiple image sets of the phantom were acquired for 5 min each starting with an air measurement and then through 2.5, 5, 7.5, 10, 12.5, 15, and 20 cm thicknesses of tissue equivalent material (Mix D, (3)). The images were acquired on a General Electric StarCam[®] scintillation camera in a 64 \times 64 word mode matrix and then down-loaded to a Macintosh[®] IIfx computer for processing. The images were digitally filtered with a Butterworth filter with a cutoff frequency of 0.25 cycles per pixel and an order

Received Nov. 19, 1991; revision accepted Feb. 20, 1992.

Address for correspondence: Christopher L. Hansen, MD, Section of Cardiology, Temple University Health Sciences Center, Philadelphia, PA 19140.

* Current Address: Dept. of Radiation Oncology, Cooper Hospital/University Medical Center, Camden, NJ.

TABLE 1
Algorithm for Attenuation Correction

1. Reconstruct low-energy peak using a heavily smoothing filter.
2. Reconstruct high-energy peak using a heavily smoothing filter.
3. Apply the regression equation to the ratio of the low- divided by the high-energy peaks from steps 1 and 2 on a pixel-by-pixel basis. This results in an attenuation correction "map" that will correct for the attenuation in the low-energy peak.
4. Reconstruct the low-energy peak using a conventional filter.
5. Multiply the low-energy reconstruction from step 4 by the attenuation correction map from step 3. This produces the corrected image.

of 10. The original low peak image was filtered again with a Butterworth filter with a cutoff of 0.5 cycles per pixel and an order of 5. Circumferential plots consisting of the maximum pixel value along each of 60 radii were calculated for the high- and low-energy images at each depth. The ratio of the counts in the low peak in air to the counts in the low peak at each depth of the less filtered low-energy image was plotted against the count ratio of the low- and high-energy images at these same depths. From this relationship, a least squares analysis was used to derive a regression equation to correct for the attenuation of the low-energy thallium counts as a function of the low-to-high count ratio. The shape of the phantom was chosen to approximate the geometry of the left ventricle. Multiple samples were taken to evaluate the variability in counts and count ratios.

Next, a simple heart phantom was created by taking ten tubes with a diameter of 1.3 cm and arranging them in a circle with an inner diameter of 3.4 cm. Thallium was diluted in water to make a concentration of approximately 1 $\mu\text{Ci/cc}$ (37 kBq/cc) to simulate the concentration of thallium in the human myocardium after exercise testing. The tubes were then filled with the diluted thallium. SPECT images were obtained with the same gamma camera and collimator used in the planar imaging study with 32 angular samples for 40 sec each over a 180° orbit. The radius of rotation was 22.5 cm to correspond to the distance used in the planar study. Simultaneous images were obtained on the same high- and low-energy peaks as the planar images in a 64 × 64 word mode format. The phantom was imaged first in air then again after immersion in a water-filled cylindrical phantom to simulate soft-tissue attenuation. It was situated eccentrically with the far edge of the heart phantom positioned close to the geometric center of the cylindrical phantom. Images were then downloaded into a Macintosh® IIfx computer for analysis. Uniformity correction was not employed.

The raw SPECT images were prefiltered with a nine-point spatial filter. Transaxial images were reconstructed using filtered backprojection with a ramp-Butterworth filter and 1-pixel thick slices. The high- and low-energy images were separately reconstructed using a Butterworth filter with a cutoff of 0.25 cycles/cm and an order of 10 (4,5). A correction factor then was determined by applying the previously described regression equation to the count ratio of the high- and low-energy images to produce an attenuation correction map.

Next, the low-energy images from the air and water data sets were reconstructed using a Butterworth filter with a cutoff of 0.35 and an order of 5. The low-energy image obtained in water was multiplied by the attenuation correction map. The counts in the air image were compared to both the corrected and uncorrected phantom image using radial profiles as described previously.

RESULTS

Figure 1 shows the results of the planar study. Sixty data points were obtained for each depth from the radial profiles. The graph depicts the log of the ratio of the low-energy counts-to-the high-energy counts versus the log of the ratio of the low counts in air divided by the low counts at depth. The measurements in air are on the left and successively greater amounts of tissue equivalent material are represented by moving to the right. The least squares regression analysis of these data yielded a slope of -0.236 and an intercept of 1.885. The standard error of the slope was 0.002 and the standard error of the intercept was 0.003. The coefficient of correlation was 0.989 and the p value was 0.0001, indicating a highly significant correlation. Since we wanted to determine the amount of attenuation as a function of the count ratio of the low and high peaks, the required regression equation is actually the inverse of the relation plotted in Figure 1 and was calculated as:

$$\ln\left(\frac{\text{low counts}_{\text{air}}}{\text{low counts}_{\text{depth}}}\right) = 7.9 - 4.2 \cdot \ln\left(\frac{\text{low counts}_{\text{depth}}}{\text{high counts}_{\text{depth}}}\right).$$

This results in the correction factor (CF):

$$\text{CF} = e\left(7.9 - 4.2 \cdot \ln\left(\frac{\text{low counts}_{\text{depth}}}{\text{high counts}_{\text{depth}}}\right)\right).$$

This correction factor was applied to the ratio of the low-to-high counts on a pixel-by-pixel basis to create the attenuation correction map which when multiplied by the low counts at depth would yield the counts in air.

Figure 2 shows representative transaxial slices for the heart phantom. The data obtained in air is on the left, the

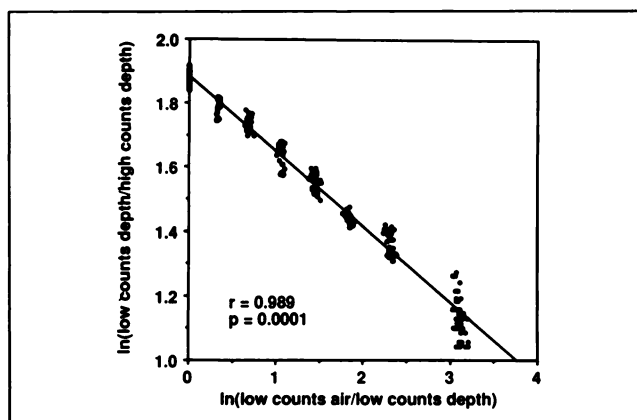


FIGURE 1. Derivation of the regression equation for the attenuation correction algorithm. The log of the ratio of the low-energy and high-energy photopeaks was measured at increasing thicknesses of tissue equivalent material and plotted as a function of the ratio of the low counts in air-to-the low counts at depth. The slope of the line is -0.236 with a standard error of 0.002. The intercept is 1.885 with a standard error of 0.003. When correcting for attenuation, the ratio of the low counts-to-high counts at depth is used to determine the ratio of the low counts at depth-to-the low counts in air—the inverse of the relation plotted here.

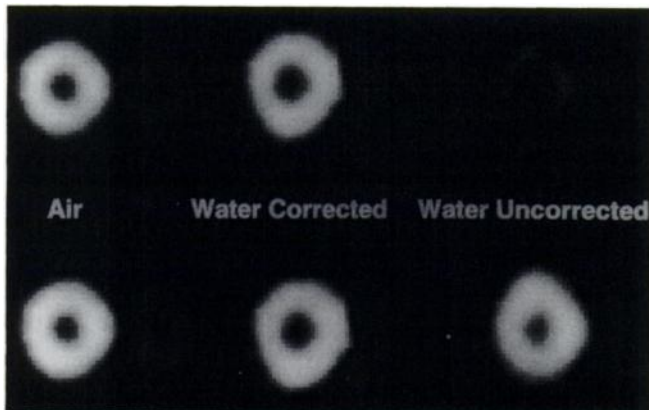


FIGURE 2. Results of attenuation correction on the heart phantom. The reconstructed images of the phantom obtained in air are shown on the left and in water on the right. The attenuation corrected images are shown in the center. The top row of images are displayed on the same gray scale and the images on the bottom are displayed normalized to the maximal pixel in each image. It can be seen that the attenuation correction corrects for the overall decrease in counts and corrects the relatively increased attenuation of the wall at 6 o'clock.

uncorrected image in water is on the right and the corrected image in water is in the center. On the top row, the images are shown on the same gray scale; on the bottom row the same three images are shown normalized to the maximal pixel in each image. It can be seen that the attenuation correction has corrected the overall decrease in counts and the relative decrease in counts in the deepest region (6 o'clock on the images). There is a minor distortion on the inferior region on the corrected image which is due to a slight overcorrection in this region.

Figure 3 shows the results of quantitative analysis of these images using radial plots. The maximum pixel was plotted along 60 radii starting at 3 o'clock on the images and moving clockwise. It can be seen that the quantifica-

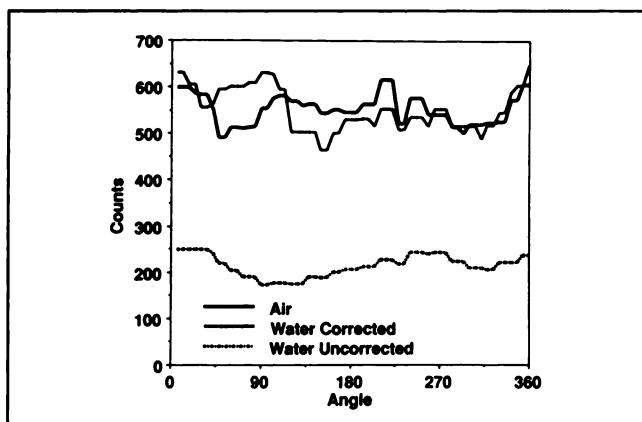


FIGURE 3. Quantitative analysis of the images in Figure 2. Radial plots were performed starting at 3 o'clock and moving clockwise. The overall 2–3-fold decrease in counts has been corrected as well as the approximately 30% decrease in counts in the wall at 90° (6 o'clock on the images).

tion of the corrected image and the image obtained in air is very close (maximum difference 21%, average difference 0.2%). The uncorrected image is plotted as well to allow comparison. This shows the attenuation correction has properly adjusted for a 2–3-fold attenuation factor and has corrected for a 31% decrease in counts in the deepest portion (6 o'clock on the images, 90° on the graph).

Figure 4 shows the results of this technique applied to a clinical image. The patient was a 40-yr-old man with a nonanginal chest pain syndrome. He was able to complete 1 min of Bruce Stage IV and achieved a peak heart rate of 182 bpm without diagnostic EKG changes. An uncorrected vertical long-axis slice is shown on the left and a corrected vertical long-axis is on the right. The images are shown on different gray scales, each normalized to its maximal pixel. The counts are roughly 2.5 times higher in the corrected image. The inferior wall can be seen to attenuate rapidly as it approaches the base on the uncorrected image. At the base of the heart, the counts are more than 30% below that at the apex. In the corresponding portion of the corrected image, the counts are within 10%.

DISCUSSION

Attenuation correction of SPECT images has always been problematic. Attempts at attenuation correction of myocardial thallium uptake using conventional techniques have not been successful due to the high attenuation of the thallium low-energy photons and the marked heterogeneity of the attenuation coefficients of the tissues surrounding the heart. More recent studies have explored iterative expectation maximum and Chang algorithms as well as Monte Carlo algorithms (6,7).

The current study is a single order post-processing correction that does not employ iterative techniques, but rather employs differences in attenuation to derive overall attenuation. The combining of iterative techniques with differential attenuation may further improve the accuracy and stability of attenuation correction.

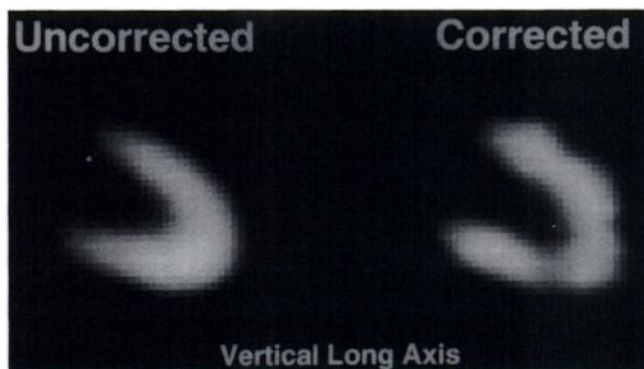


FIGURE 4. Results of this technique applied to a 40-yr-old man with a low pre-test probability for CAD. There is significant attenuation of the inferior wall as it approaches the base on the uncorrected image that has been markedly reduced on the corrected image.

Other investigators have attempted attenuation correction using differential attenuation. Martin and Rollo were able to successfully correct attenuation of the thyroid by calculating the differential attenuation of the 159 and 28 keV photopeaks of ^{123}I (8). The Compton scatter occurred mainly in the 80 keV range and did not interfere with the low-energy peak. Although this technique may work for the thyroid, it is unlikely that enough photons from the 28 keV peak would be available from organs lying deeper than the thyroid to enable it to be used successfully. Van Rensburg and colleagues were not able to successfully employ differential attenuation using ^{111}In due to the significant downscatter of the 247 keV peak into the 172 keV peak (9).

Thallium-201 seems ideally suited for the analysis of differential attenuation. Correction using differential attenuation will be problematic when there is significant downscatter from the high peak into the low peak. However, since the number of low-energy photons with thallium is much greater than the number of high-energy photons, the relative downscatter contribution from the high peak into the low energy window is quite small. Furthermore both energy peaks are within the range that can be imaged with a low-energy collimator and they are of sufficiently different energy to allow for separate imaging.

Other investigators have used dual-window techniques for improving SPECT images (10,11). In each of these investigations, a second window was acquired with the energy centered over the Compton peak. These techniques have shown promise for scatter correction but have not been developed for correction of attenuation.

Due to the fact that this technique first divides two images and then exponentiates the result, it is very susceptible to image noise. The contributions due to noise can be reduced by using a high degree of filtering for the generation of the attenuation correction map. It appears that this technique does not suffer dramatically by heavy filtering, probably due to the fact that in three dimensions, attenuation is a very low spatial frequency phenomenon. Therefore, a low frequency attenuation correction map can be generated and then applied to a less filtered image. In our experience, the choice of the filter depends on a trade-off between image noise and loss of spatial resolution. We have preferred the heaviest filters possible.

The images in this study were not uniformity corrected. We feel that this technique would be optimized if the low-energy peak were corrected with a thallium uniformity flood. There is some residual low frequency artifact in the corrected images that might be reduced by this. The high energy peaks could probably be accurately corrected with a cobalt uniformity.

The accuracy of this technique will also depend on the energy resolution of the camera being used. The system we used had an energy resolution of 14% on the low-energy peak. Further refinement may occur with detectors

that have better energy resolution, such as semiconductor detectors.

We conclude that the differential attenuation of thallium photons allows for the attenuation correction of thallium images. This may reduce attenuation artifacts found in thallium imaging and allow for the more accurate assessment of patients with known or suspected CAD.

APPENDIX

Theory of Attenuation Correction

For the low (l) and high (h) energy peaks:

$$C_l = C_l^* e^{-\mu_l d} \quad \text{Eq. 1}$$

$$C_h = C_h^* e^{-\mu_h d} \quad \text{Eq. 2}$$

Dividing Equations 1 and 2 gives

$$C_l/C_h = (C_l^*/C_h^*) e^{-(\mu_l - \mu_h) d} \quad \text{Eq. 3}$$

Solving for depth d

$$d = [\ln(C_l^*/C_h^*) - \ln(C_l/C_h)] / (\mu_l - \mu_h) \quad \text{Eq. 4}$$

and substituting into Equation 1 yields the regression relationship:

$$\ln(C_l^*/C_l) = [\mu_l/(\mu_l - \mu_h) * \ln(C_l^*/C_h^*) - [\mu_l/(\mu_l - \mu_h)] * \ln(C_l/C_h).$$

The correction factor is then given by:

$$CF = e ([\mu_l/(\mu_l - \mu_h) * \ln(C_l^*/C_h^*) - [\mu_l/(\mu_l - \mu_h)] * \ln(C_l/C_h)].$$

The corrected image is obtained by multiplying the low-energy counts at depth by the correction factor.

ACKNOWLEDGMENT

Supported in part by Biomedical Research Support grant #RR05417.

REFERENCES

1. Garcia EV, Van Train K, Maddahi J, et al. Quantification of rotational thallium-201 myocardial tomography. *J Nucl Med* 1985;26:17-26.
2. Tamaki N, Yonekura Y, Mukai T, et al. Stress thallium-201 transaxial emission computed tomography: quantitative versus qualitative analysis for evaluation of coronary artery disease. *J Am Coll Cardiol* 1984;4: 1213-1221.
3. Jones DEA, Raine HC. Letter to the editor. *Br J Radiol* 1949;22:549.
4. Shepp LA, Logan BF. The fourier reconstruction of a head section. *IEEE Trans Nucl Sci* 1974;NS-21:21-43.
5. Kak AC, Slaney M. *Principles of computerized tomographic imaging*. New York: IEEE Press; 1987.
6. Tsui BMW, Gulberg GT, Edgerton ER, et al. Correction of nonuniform attenuation in cardiac SPECT imaging. *J Nucl Med* 1989;30:497-507.
7. Ljungberg M, Strand S. Scatter and attenuation correction in SPECT using density maps and Monte Carlo simulated scatter functions. *J Nucl Med* 1990;31:1560-1567.
8. Martin PM, Rollo FD. Estimation of thyroid depth and correction for I-123 uptake measurements. *J Nucl Med* 1977;18:919-924.
9. van Rensburg AJ, Lötter MG, Heyns A, Minnaar PC. An evaluation of four methods of In-111 planar image quantification. *Med Phys* 1988;15: 853-861.
10. Jaszczak RJ, Greer KL, Floyd CE, Harris CC, Coleman RE. Improved SPECT quantification using compensation for scattered photons. *J Nucl Med* 1984;25:893-900.
11. Koral KF, Swailen FM, Buchbinder S, Clinthorne NH, Rogers WL, Tsui BMW. SPECT dual-energy-window Compton correction: scatter multiplier required for quantification. *J Nucl Med* 1990;31:90-98.